Laboratory Measurement of the X-ARAPUCA's Absolute Photon Detection Efficiency for the Deep Underground Neutrino Experiment's Vertical Drift Far Detector

- G. Botogoske^{b,3,4}, F. Bruni⁵, E. Calvo¹, R. Calabrese^{2,3}, N. Canci³,
- A. Canto¹, C.M. Cattadori⁵, A. Cervera Villanueva⁸, S. Coleman⁹,
- J.I. Crespo-Anadón¹, C. Cuesta¹, F. Di Capua^{2,3}, N. Durand⁹,
- G. Fiorillo^{2,3}, F. Galizzi^{5,6}, I. Gil-Botella¹, C. Gotti⁵, G. Grauso³,
- J. Jablonski⁹, A.A. Machado⁷, S. Manthey Corchado^{a,1}, J. Martín–Albo⁸,
- G. Matteucci^{2,3}, L. Meazza^{5,6}, A.P. Mendoça⁷, A. Minotti^{5,6},
- D. Navas-Nicolás¹, L. Pagliuso⁷, C. Palomares¹, L. Pérez-Molina¹,
- V. Pimentel⁷, I. López de Rego¹, Z. Rautio⁹, J. Romeo-Araujo¹,
- D. Rudik^{2,3}, E. Segreto⁷, Y. Suvorov^{2,3}, M. Sturdivant⁹, F. Terranova⁵,
- J. Ureña⁸, A. Verdugo de Osa¹, D. Warner⁹, R. Wilson⁹, K. Zhu⁹
- ¹ Centro de Investigaciones Energéticas Medioambientales y Tecnológicas (CIEMAT), 28040 Madrid (Spain)
- ² Università degli Studi Federico II, Dipartimento di Fisica, 80126 Napoli (Italy)
- ³ Instituto Nazionale di Fisica Nucleare, Sezione di Napoli, 80126 Napoli (Italy)
- ⁴ University of Padova, 35121 Padova (Italy)
- ⁵ Instituto Nazionale di Fisica Nucleare (INFN), Sezione di Milano Bicocca, 20126 Milano (Italy)
- ⁶ University of Milano Bicocca, 20126 Milano (Italy)
- ⁷ University of Campinas (Unicamp), 13083-852 Campinas (Brazil)
- ⁸ Instituto de Física Corpuscular (IFIC), CSIC-Universitat de València, Paterna 46980 (Spain)
- ⁹ Colorado State University, Colorado 80523 (USA)

Received: date / Accepted: date

Abstract The Deep Underground Neutrino Experiment (DUNE) will probe fundamental questions in particle physics and cosmology. Its Far Detectors implement a Photon Detection System composed of light-sensitive devices called X-ARAPUCA (XA). These trap incoming VUV photons by total internal reflection in a Wavelength Shifter Light Guide to be collected onto wrapping Silicon Photomultiplier arrays, sensitive to visible light. In the baseline design, Dichroic Filters (DFs) are implemented to improve the collection efficiency of escaping photons. The configuration proposed for DUNE's Vertical Drift module has been characterised in Liquid Argon for the first time using dedicated cryogenic setups developed at CIEMAT and INFN Naples. Additionally, several alternative configurations, based on the design optimisation studies of an R&D campaign, have been evaluated. The results show an efficiency of up to 4.5 ± 0.4 % at 4.5 V overvoltage, representing a high improvement with respect to previous XA implementations. Most noticeably, configurations

Keywords Noble Liquid Gas detectors · Cryogenic Detectors · UV Detectors · Neutrino detectors

1	Intr	$\operatorname{oduction} \ldots \ldots \ldots \ldots \ldots \ldots$
	1.1	XA concept for DUNE
	1.2	XA Simulation
	1.3	General PDE Computation
2	Refe	erence Method
	2.1	Characterization Box
	2.2	Computation Strategy
	2.3	XA Configurations
3	Sim	ulation Method
	3.1	Setup Simulation
	3.2	Computation Strategy
4	Data	a Analysis & XA Characterization 12
	4.1	XA Calibration
	4.2	Scintillation Charge Analysis
5	Resi	ılts
	5.1	Baseline PDE XA Results
	5.2	Stability & Repetitivity 16
	5.3	XA Configuration Comparison
6	Con	clusions

without DFs show an improvement of up to 18 \%,

which has been attributed to transmittance deficits.

Contents

^ae-mail: sergio.manthey@proton.me

^be-mail: gabriel.botogoske@studenti.unipd.it

1 Introduction

The Deep Underground Neutrino Experiment (DUNE) is a next-generation dual-site experiment [1] that aims to measure the neutrino oscillation parameters with unprecedented precision, allowing the measurement of CP violation in the leptonic sector and the neutrino mass ordering [2]. It can perform nucleon decay and other beyond the standard model searches as well as detect astrophysical neutrinos from the Sun and core collapse supernovae within our galaxy [3]. DUNE's Far Detector (FD) consists of four 17 kt Liquid Argon Time Projection Chamber (LArTPC). The first FD module to be installed is designed to implement the Vertical Drift (VD) technology, in which ionisation charges are drifted perpendicularly from a central cathode to two anode planes. This generates two fiducial volumes (top and bottom) of approximately 7 m in drift distance. A schematic representation of this Time Projection Chamber (TPC) is shown in Figure 1.

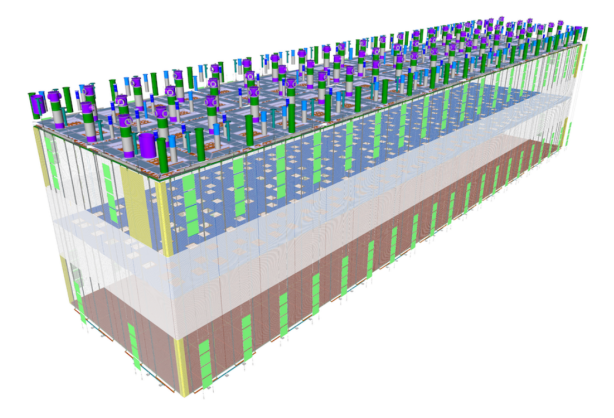


Fig. 1 Design for DUNE's VD FD module. Showing cathode X-ARAPUCAs in grey and membrane X-ARAPUCAs in green. The anode planes are shown in brown. The TPC is surrounded by a field cage, which is made semi-transparent for visual purposes.

The Photon Detection System (PDS) of DUNE's FD VD module consists of thin (60 cm × 60 cm) light collector devices, called X-ARAPUCA (XA) [4], which are placed in the cathode structure (320 XAs) and the membrane at the inner sides of the cryostat walls (352 XAs outside the field cage). Due to the transparent nature of the VD's cathode, this first set of modules needs to be sensitive to the light produced in both drift regions, requiring both their surfaces to be active, or Double-Sided (DS). On the other hand, the modules mounted on the membranes need to be insensitive to the light produced behind them, outside of the active volume, requiring one side of the module to be opaque, or Single-Sided (SS). Additionally, in order to avoid elec-

tric interference with the high–voltage field, the cathode XAs require novel power– and signal–over–fiber technologies that allow for the supply and readout of the XAs [5].

Liquid Argon (LAr) is an ideal target for neutrino detection because interacting particles generate ionisation charge $(42\,000\,e^{-}{\rm MeV}^{-1})$ and abundant Vacuum Ultraviolet (VUV) scintillation light $(51\,000\,\gamma \text{MeV}^{-1})^1$ [6,7]. The particle's energy deposits generate singlet and triplet states of Ar dimers (Ar₂) that de–excite with characteristic times $\tau_{\rm fast} = 7.1\,{\rm ns}$ and $\tau_{\text{slow}} = 1.66 \,\mu\text{s}$ emit VUV (127 nm) photons [8]. This prompt light signal provides the triggering and interaction time for non-beam events, such as supernovae and solar neutrinos, additionally improving the reconstruction capabilities of all experimental measurements. In order to evaluate the performance of the PDS, the Light Yield (LY), defined as the total Photoelectron (PE) count detected onto the PDS per energy deposit, is the main figure of merit to be considered. To fulfil the scope of DUNE's physics program, an average LY of $20 \,\mathrm{PE}\,\mathrm{MeV}^{-1}$ is required. This can can be achieved for the nominal XA arrangement (6% surface coverage) with a Photon Detection Efficiency (PDE) > 3% [9].

This work presents the absolute calibration and characterisation results of the XA device in a cryogenic LAr environment for DUNE, performed by two research institutions: Centro de Investigaciones Energéticas Medioambientales y Tecnológicas (CIEMAT) in Madrid and Instituto Nazionale di Fisica Nucleare (INFN) in Naples. Each institution has developed its own PDE measurement to ensure the reliability of the results presented for the baseline XA design. Additionally, a purposely chosen set of different XA configurations has been measured at CIEMAT to inform on the design developments.

This Section 1 describes the implementation of the XA concept to DUNE's VD FD module. In Sections 2 and 3, both PDE computation strategies and the corresponding cryogenic setups and measurement strategies are described. Section 4 shows the basic calibration steps of a typical photosensor device. Section 5 provides a comprehensive description of the PDE measurements for the baseline XA and analyses the PDE improvements by comparing all XA configurations measured at CIEMAT. Finally, Section 6 concludes with this work's main observations aiming to improve the XA baseline.

¹Values vary in the presence of an electric drift field.

SINGLE - SIDED X-ARAPUCA

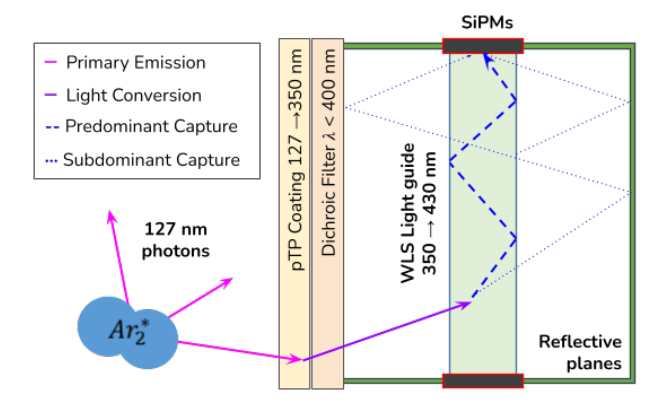


Fig. 2 Schematic of the XA working principle [10]. Not to scale.

1.1 XA concept for DUNE

The XA photosensor device is a novel design developed by the DUNE collaboration to detect scintillation light in the LAr TPCs of the far detector modules. The XA is a compact, modular and scalable device that can be adapted to different configurations and applications. It is designed to operate at cryogenic temperatures, and it is capable of detecting VUV scintillation light with low noise. Its goal is to maximise the surface coverage of the PDS while minimising the amount of expensive Silicon Photomultiplier (SiPM)s required to achieve the desired PDE.

The XA entrance window is covered by a substrate coated on the external side with a p-Terphenyl (pTP) layer ($\sim 500 \, \mu \mathrm{g \, cm^{-2}}$) to convert the incident 127 nm scintillation light into isotropically re-emitted 350 nm photons with a high efficiency [11]. The re-emitted light reaches the acrylic (polymethyl methacrylate) Wavelength Shifter Light Guide (WLS-LG) where it is further downshifted and isotropically re-emitted to the visible range (430 nm) thanks to the doping with chromophore (see Figure 2). The current baseline lightguide is a Polymethyl Methacrylate (PMMA) bar of 3.8 mm thick and has a 80 mg kg⁻¹ chromophore concentration (see Table 1). The WLS-LG re-emitted light can be trapped by total internal reflection (critical angle $\theta \sim 56^{\circ}$) and reach the surrounding SiPM arrays or escape and be reflected back into the WLS-LG by a thin-film dichroic filter coating, whose cutoff is should be above $400\,\mathrm{nm}$ for 45° angle of incidence. The nonactive surfaces of the XA are covered with a highly reflective film (VIKUITI^T[12]) to reduce the absorption of the escaping photons and redirect them to the WLS-LG for enhanced collection probability. The XA technology has demonstrated its superior PDE compared to dip-coated shift light guides (whether SS or DS) [13].

	Wavelength	Shifter	Light	Guide	Summary
--	------------	---------	-------	-------	---------

WLS-LG	Length x Height x Width	Chromophore
A B	$605\mathrm{mm}\times605\mathrm{mm}\times3.8\mathrm{mm}$ $607\mathrm{mm}\times605\mathrm{mm}\times5.5\mathrm{mm}$	$80 \mathrm{mg}\mathrm{kg}^{-1}$ $24 \mathrm{mg}\mathrm{kg}^{-1}$

Table 1 Tested WLS–LG configurations. A being the baseline configuration and B the alternative designed to improve the PDE. The chromophore concentration is given in $\mathrm{mg}\,\mathrm{kg}^{-1}$ of the acrylic substrate.

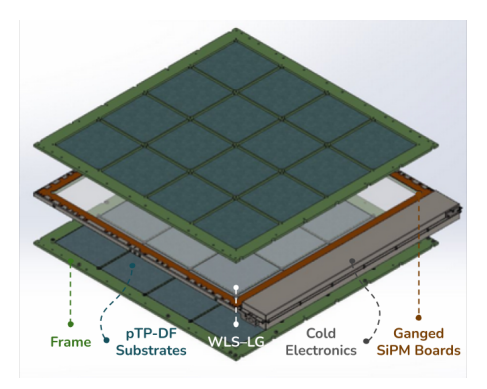
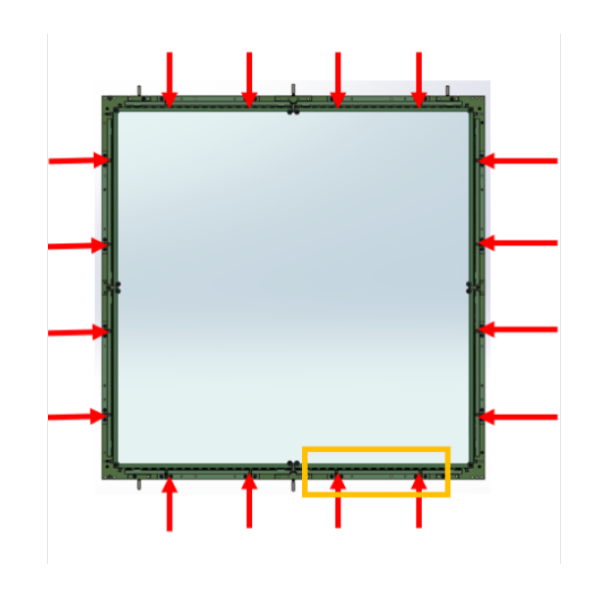


Fig. 3 Scheme of the XA concept implementation for DUNE'S VD FD module. Displayed are the substrate and WLS-LG layers, where the first can be seen surrounded by the XA mounting frame and the latter by the SiPM strips and spring-loaded mechanism.

Figure 3 shows the XA implementation and design for the VD, whose surface is covered by 16 pTP-coated Dichroic Filter (DF)s. In all cases, 160 SiPMs are mounted on 8 flex-boards (covered with VIKUITI) and positioned around the WLS-LG (from G2P [14]). These SiPMs (model FBK Triple-Trench [15]) have an active area of $6 \times 6 \,\mathrm{mm}^2$. All these main components are encased in the XA mechanical frame, which consists of brackets holding the different components in place. A spring-loaded mechanism (see Figure 4) ensures optimal contact between the SiPM active surfaces and the WLS-LG edges, counteracting the cryogenic contraction of the system. With respect to the design described in DUNE's Technical Design Report (TDR) [9], the mechanical frame of the XA's baseline design underwent some modifications. Most noticeably, four clamping brackets were added to the frame to mitigate the WLS-LG misalignment under bending conditions, which can be caused during horizontal assembly, storage or transportation. This change was not implemented in the XA prototype measured by the INFN Naples team, requiring a custom bending correction to the analysis (see Section 3.2). The resulting misalignment between the WLS–LG and the SiPMs was not present in CIEMAT's measurements, thanks to the aforementioned mechanical improvements and the vertical orientation during data–taking.



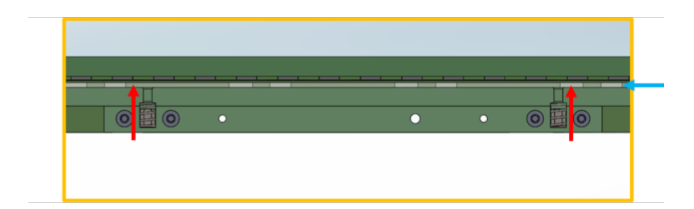


Fig. 4 Schematic representation of the VD XA spring—loaded mechanism. SiPMs are mounted between the WLS-LG and an acrylic interface strip (blue arrow). Springs (red arrow) apply constant pressure orthogonal to this interface. Thermal shrinkage at cryogenic temperatures of the WLS-LG is 6 mm, which causes the springs to partially decompress to 11.5 mm. These springs are mechanically constrained to exert force and translate solely orthogonal to the WLS-LG face. This design enables SiPMs to translate in unison with WLS-LG shrinkage toward the centerline.

The XA readout–system comprises two amplifier stages (cold and warm). The mounted SiPMs are ganged in groups of five and deliver output data across two channels connected to the readout cold–amplifier. The signals are routed to the front–end electronics by custom–designed signal leading–boards [16]. This cold stage is composed of a main board with two cold

transimpedance amplifiers , which are responsible for the active ganging of the SiPMs. Each input reads 80 SiPMs (half of the XA). The cold amplifier is held inside a metal casing mechanically attached to one side of the XA (see Figure 3).

1.2 XA Simulation

In order to estimate the device's response to the different optical components and to inform about the specific XA configuration to be tested (see Section 2.3), a custom—made Monte Carlo (MC) simulation of the whole XA has been developed to compute the device's Photon Collection Efficiency (PCE). This simulation—derived performance value differs from the previously defined PDE as it does not account for the experimental reconstruction process evaluated through this work. Nevertheless, this simulation implements the measured optical properties of all active components and derives the fraction of collected photons onto the SiPMs active surface area.

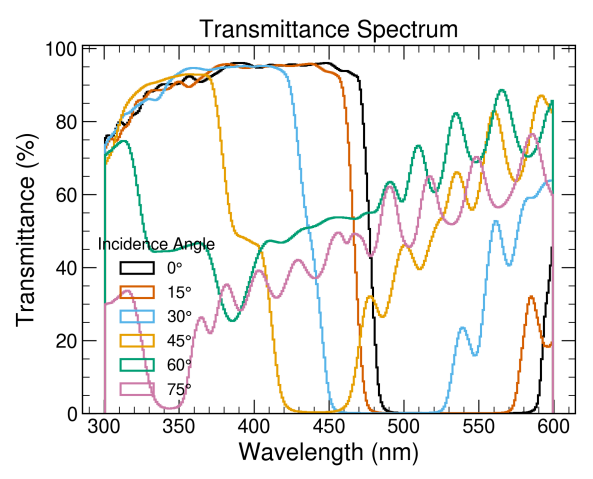


Fig. 5 DF transmission curves from ZAOT measured in demineralised water for different angles of incidence.

The most relevant results concern the impact of the dichroic filters, whose transmittance curves are inevitably shifted in wavelength depending on the angle of incidence (see Figure 5). The aforementioned simulation, which has been adapted to extrapolate experimental transmittance curves to reproduce custom cutoff positions, suggests that this parasitic effect causes realistic dichroic filters to reduce the PCE of the XA.

Independently, experimental studies performed at INFN Pavia in a vacuum chamber equipped with a Deuterium lamp and a monochromator have shown that pTP evaporated ZAOT glass substrates with a DF back

coating have a $\sim 30\%$ decrease in detected light when irradiated with a 127 nm light source compared to non–DF coated samples [17].

Both these studies have motivated the measurement of XAs without DFs as a means to improve their PCE (see Section 2.3). Experimentally, the improvement in detector performance driven by these design changes can be evaluated by computing the PDE for each configuration.

1.3 General PDE Computation

The PDE is computed as the number of PEs measured by the photosensor device with respect to the true number of incident photons arriving at its surface $(\epsilon_{XA} = PE_{XA}/\gamma_{true})$. In the Sections 2 and 3 we will distinguish between two computation strategies: reference and simulation. These differ on the approach of measuring the true number of incident photons. Experimentally, these two conceptual methods have been realized by constructing two cryogenic setups that illuminate the XA device with a radioactive ²⁴¹Am source that emits alpha particles of known energy. In the reference method this true value is obtained from a reference SiPM with known efficiency and a geometric factor that accounts for the different active surfaces of the sensors and their relative positions. This method has the advantage of being insensitive to global bias effects of the absolute light that could be introduced by the simulation artifacts or LAr impurities. The disadvantage is that the uncertainty in the reference SiPM's efficiency is directly propagated to the XA (as will be shown in Section 5). Crucially, these uncertainties are cancelled when comparing among different XA configurations. In the case of the simulation method, the true number of incident photons is computed from a custom MC simulation that takes into account the full geometry of the XA. This method is very sensitive to changes in the absolute amount of scintillation light that can be affected by hardly detectable impurities in the LAr. Therefore, a purification system and an analytical purity correction are needed to ensure that real setup measurements agree with the light production expected from the sim-

In both PDE computation methods the number of true collected PEs (PE_{XA}) is computed from the number of detected PEs (PE_{XA}') and the Crosstalk (XT) correction factor as follows:

$$PE_{XA} = \frac{Q^{0}}{SPE^{0} \cdot (1 + K_{dup}^{0})} + \frac{Q^{1}}{SPE^{1} \cdot (1 + K_{dup}^{1})}$$

$$\approx \frac{Q^{0} + Q^{1}}{\langle SPE \rangle} \cdot \frac{1}{1 + \langle K_{dup} \rangle} \equiv PE'_{XA} \cdot f^{XT}$$
(1)

where Q^0 and Q^1 correspond to the mean charge of the scintillation runs for each XA channel; SPE⁰ and SPE¹ are the corresponding Single Photoelectron (SPE) charge values and $K^0_{\rm dup}$ and $K^1_{\rm dup}$ are the cross-talk (XT) duplication factors , since SiPMs exhibit a significant probability of a secondary pulse occurring caused by the emission of infrared radiation in a SPAD pixel or the presence of trapped impurities. The procedure used to determine the (XT) duplication factors is described in more detail in Equation 11. Both XA channels are identical in terms of SiPM number and readout connections and therefore present compatible calibration results. Therefore, the channel dependency has been removed from the equations, as the measurement's uncertaty is bigger than the spread in global SiPM response.

2 Reference Method

At CIEMAT, the XA is submerged vertically in LAr together with three characterisation boxes hosting a low-activity electrodeposition—coated ²⁴¹Am source and two reference SiPMs [18]. This ensures the PDE being assessed at Cryogenic Temperature (CT) and with 127 nm incident light to reproduce the operating conditions of the DUNE experiment.

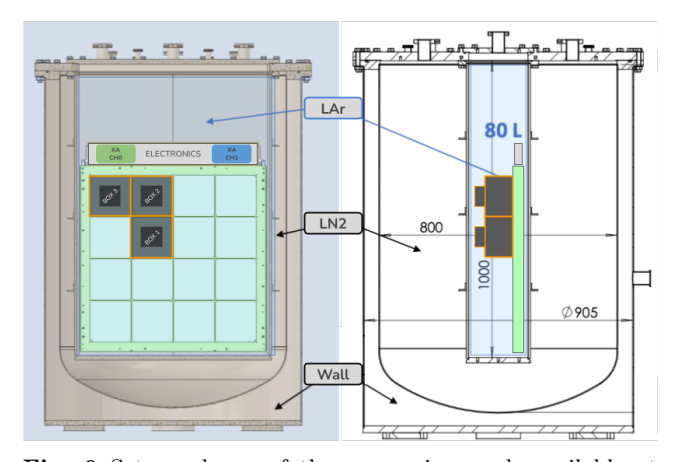


Fig. 6 Setup scheme of the cryogenic vessels available at CIEMAT for the XA's absolute efficiency measurement.

The setup consists of a $\sim 300\,\mathrm{L}$ cylindrical vessel with a squared cassette ($\sim 80\,\mathrm{L}$) that hosts the XA (see Figure 6) where grade 6.0 Gaseous Argon (GAr) can be liquified. The larger and external volume is filled with Liquid Nitrogen (LN₂) during data campaigns to serve as a cold reservoir for the inner volume. Before a run of data taking, successive vacuum cycles ($< 1 \times 10^{-4}\,\mathrm{mbar}$) are performed to avoid outgassing of the setup components during the filling process, which might worsen

the LAr purity. The GAr liquification happens by thermal contact with the $\rm LN_2$ reservoir. The setup is designed to maintain constant operating conditions. This is achieved with a slow control system that reads the output of electronic pressure valves to regulate filling electro–valves that perform the filling of the $\rm LN_2$ reservoir from a 450 L tank which is at an over–pressure of 7.2 bar, while the GAr is maintained at 2.7 bar. The liquification of the GAr is monitored by PT100 temperature sensors that provide live temperature readings of the LAr level inside the vessel.

Each XA configuration is tested in data campaigns lasting three days to ensure data stability and repetitiveness, with the whole setup preparation lasting over a week. The data transmission chain and Data Acquisition (DAQ), involving the warm–amplification stage and the read–out system, are schematically represented in Figure 7.

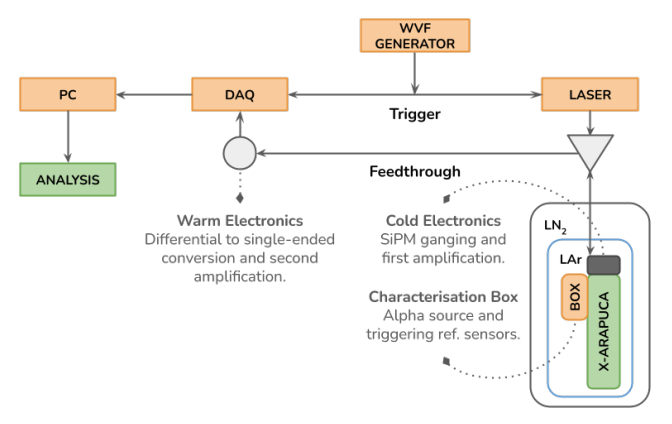


Fig. 7 Schematic representation of the data flow during data acquisition.

2.1 Characterization Box

As described above, the XA is introduced together with three characterisation boxes (see Figure 8), one for each of the uniquely distinct substrate—window position of the XA. Each of these boxes hosts two reference HPK VUV4 SiPMs (S13370–6075CN) [18] which are designed to have a high sensitivity for VUV light and stable performance at CT, making it possible to directly detect the scintillation light produced in LAr by alpha particles emitted from the radioactive ²⁴¹Am source. Regarding the reference SiPMs, studies have shown an efficiency decrease of about 50% in CT with respect to the PDE measured by the manufacturer at RT [19]. Therefore, measurements carried out previously at CIEMAT have been necessary to compute a reference PDE of

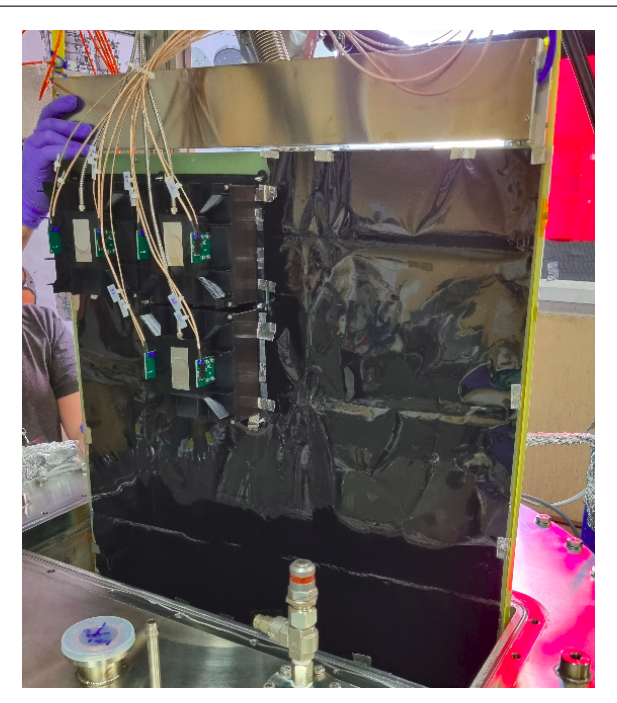


Fig. 8 Insertion of an XA inside the cryogenic vessel.

 $(12.69\pm1.12)\%$ for 127 nm at 87 K and 4 V Overvoltage (OV) [20]. These results together with the crosstalk probability (P_{XT}), estimated at CIEMAT using the Vinogradov method [21] from calibration data (see Section 4), and the PDE dependence with the incident angle [22] provide a characterisation of these SiPMs. The main calibration results of these reference sensors are listed in Table 2.

HPK VUV4 (reference SiPMs)

OV(V)	Gain $(\cdot 10^6)$	S/N	$P_{\rm XT}$ (%)
3.0	6.0 ± 0.2	6.3 ± 1.4	18 ± 2 25 ± 3 33 ± 4
4.0	8.0 ± 0.3	6.5 ± 2.1	
5.0	10.1 ± 0.5	6.9 ± 2.6	

Table 2 Reference SiPMs calibration results at 87 K and 127 nm light. The gain and the signal–to–noise ratio (S/N) are computed from the charge of the SPE spectrum. The XT probability ($P_{\rm XT}$) is estimated from the same calibration data using the Vinogradov method [21].

Together with the reference detectors, the 241 Am source is held inside a black box (as shown in Figure 10). The emitted α -particles have two main energies 5.485 MeV (84.45%) and 5.443 MeV (13.23%) with an activity of (54.53 \pm 0.82) Bq [23]. The particles deposit their energy onto the LAr and produce photons that reach the XA and the reference sensors. To ensure that no other photons are detected, a black sheet covers the rest of the XA (see Figure 8). An optical fiber guides light from an external laser source that can be operated

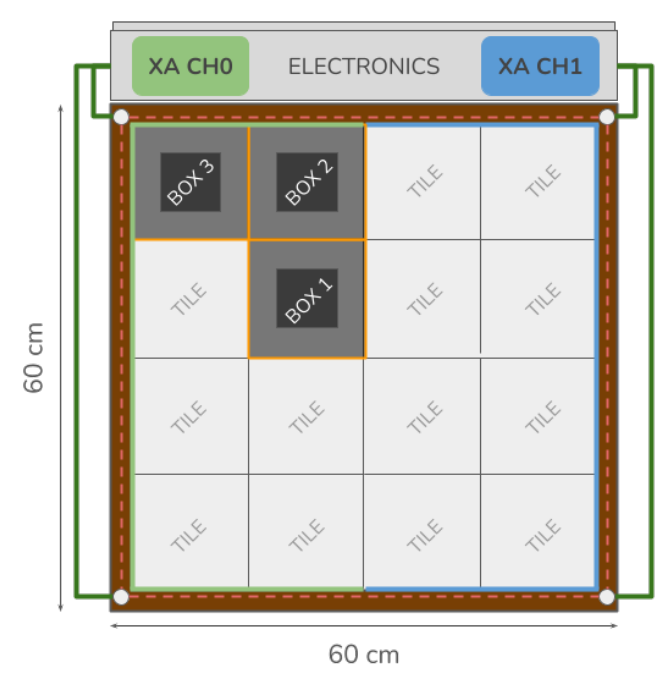


Fig. 9 Schematic representation of the XA with channel arrangement and filter positions.

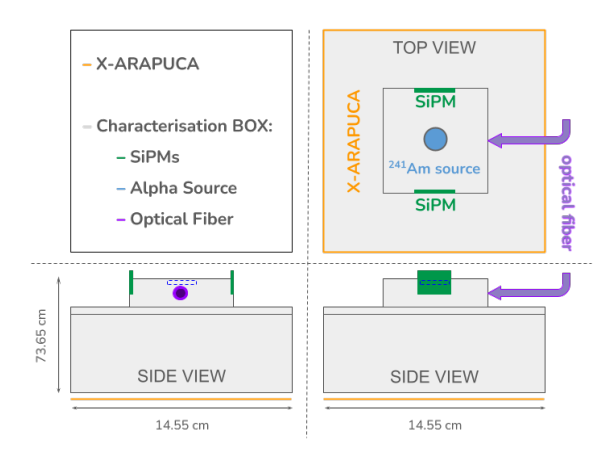
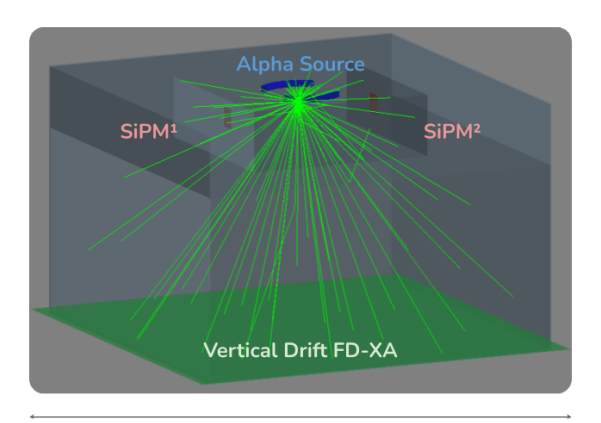


Fig. 10 Characterisation box hosting the reference sensors together with the ²⁴¹Am source and the inlet for the optical fiber used in calibration.

by a waveform generator (see Figure 7), providing simultaneously a precise and sharp pulse of light and the appropriate trigger to the DAQ (CAEN DT5725 [24]). The response of the system to the external light pulse is used to characterise the sensors. Table 3 shows the sensors' dimensions and positions in the box with respect to the alpha source, which have been meticulously chosen to ensure an appropriate illumination of the active surfaces with a Geant4 simulation.



14.55 x 14.55 cm²

Fig. 11 MC simulation of the characterisation box tracking 100 photon trajectories.

2.2 Computation Strategy

This Geant4 simulation of the characterisation box is a necessary resource for designing and understanding the geometry and signal distributions of the characterising setup. Most importantly, its design has been studied to avoid the shadowing of the inner surfaces and allow light produced by the alpha particles to propagate directly to the different sensitive areas.

Parameters	Input/Output	XA	Ref. SiPM
Distance to Source (mm)	input	74	29
Effective area (mm ²)	input	211.7	36
Collected Photons	output	25900	603
Average Incidence Angle (°)	output	90°	75°

Table 3 Simulation parameters from the characterisation box simulation.

Figure 11 shows the simulated geometry. The walls of the characterisation box are 3D–printed from a black plastic material that fully absorbs the photons (here shown semi–transparently for illustration purposes). The source holder is displayed in blue. The two reference VUV4 SiPMs (red) and the XA (green) are also highlighted in colours and configured as sensitive areas to retrieve the number of photons.

For this reference method, the true number of incident photons (as predicted by the simulation) can be expressed in terms of the PEs detected by the reference SiPMs ($\gamma_{\rm true} = {\rm PE_{ref.}}/\epsilon_{\rm ref.}$). Therefore, the corresponding PDE computation method can be formulated as follows:

$$PDE_{XA}^{reference} = \frac{PE_{XA}' \cdot f_{XA}^{XT}}{PE_{ref}' \cdot f_{ref}^{XT}} \cdot \epsilon_{ref.} \cdot f^{geo}, \qquad (2)$$

for which f^{geo} , the ratio of the geometrical acceptances per unit area, has been evaluated with a custom simulation (see Section 2.1).

Instead of simulating alpha particles directly, the software generates exactly 195 636 γ (corresponding to a light yield of 51 000 γMeV^{-1} and a quenching factor of 0.7) and places them at a random position over the source's radiative surface. These photons are propagated uniformly and isotropically across the LAr volume. The simulation provides the number of photons reaching the XA acceptance window as well as the reference SiPM sensors, which resulted in $25\,900\pm238$ and $603 \pm 7 \gamma$, respectively. Additionally, the resulting data provides the average incidence angle of all collected photons. This is used to correct the reference SiPM PDE from the previously cited value to $12.1 \pm 1.1\%$, by using the cited angle dependence of the PDE. The geometrical correction factor of Equation 2 is also evaluated from this simulation:

$$f^{\text{geo}} = \frac{\text{MC}_{\text{ref.}}^{\text{photons}}}{\text{MC}_{\text{XA}}^{\text{photons}}} = 0.0465 \pm 0.0007.$$
 (3)

With the previously introduced definition of the reference method in Equation 2 and the factors extracted from the characterisation box simulation, the remaining parameter to address is the number of detected photons by the reference sensors ($PE'_{ref.}$). Due to their position inside the box, one expects an average incidence angle distribution that is not perpendicular. This has already been accounted for by correcting the reference PDE. An additional side-effect of the arrangement and the non-negligible extension of the source, whose diameter is 22 mm), is the asymmetric response of each single SiPM sensor. This response is well predicted by simulation, so MC data has been used to feed a fitting function that convolves the true photon distribution with a Poisson probability in each bin. The minimised parameter in this case is the reference SiPM's efficiency, which can be used as a cross-check to ensure the correct implementation of the simulation. From this procedure, one obtains an SiPM efficiency value of $9.2 \pm 0.4\%$ (see Figure 12). This agrees well with the forementioned value taking into account that the LY decrease caused by impurities in the LAr are not accounted for in this computation.

The combined response of both SiPMs provides a symmetric distribution. This can be Gaussian–fitted to extract the average charge of the scintillation light for the alpha–runs. It is important to notice that, contrary to the two channels of the XA, these SiPMs can have slightly different gains. Therefore, their individual signals are first calibrated, then integrated in charge, and finally converted to PE count before combining the data into a summed distribution.

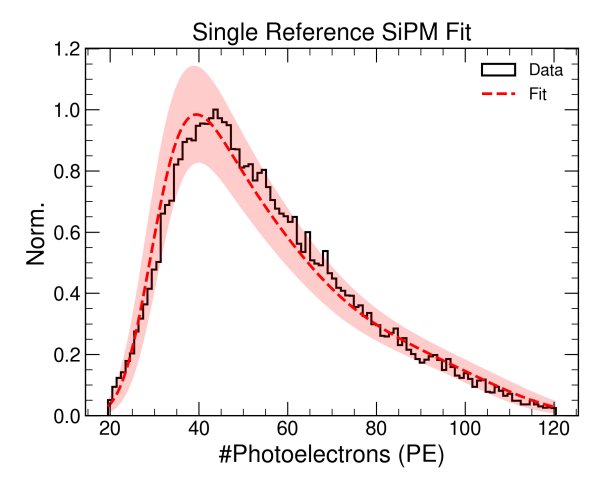


Fig. 12 Fitted SiPM response to MC model. The red band represents the propagated uncertainty in the fit.

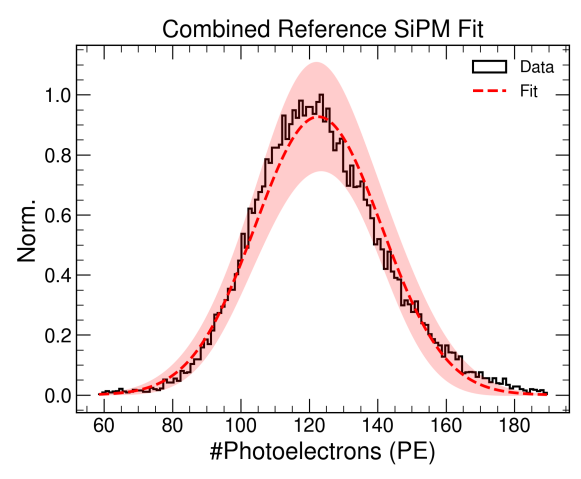


Fig. 13 Fitted combined SiPM response from characterisation box 2.

An example of a combined reference SiPM fit can be seen in Figure 13. The reference SiPMs have always been operated at the same OV, ensuring that the PDE is computed under the same conditions. Additionally, the required trigger coincidence of these sensors ensures that the DAQ only records true signal events, providing a cleaner sample of the alpha particles' scintillation light.

2.3 XA Configurations

As mentioned in Section 1, the simulation—supported R&D and optimisation efforts have motivated the study of different XA configurations. The predicted improvement in PDE for a configuration without DF has been assessed with the production of pTP—coated substrates without the addition of dichroic layers. These have been mounted and tested for both

Single— and Double—Sided configurations of the XA. Additionally, the WLS—LG width and chromophore concentration have been studied to evaluate their impact on the efficiency. Two WLS—LG designs have been produced by G2P, presented in Table 1. Table 4 shows the list of all tested XA configurations. It is important to mention that the single-sided XA with dichroic filters has been measured in two campaigns to reduce the statistical errors and improve the comparison with the simulation method.

X-ARAPUCA Configurations

	Configuration	Filter	Substrate	WLS-LG	Type
1	DF-XA	Yes	ZAOT	A	Single-Sided
2	DF-XA-DS	Yes	ZAOT	A	Double-Sided
3	noDF-XA	No	P.E.	A	Single-Sided
4	noDF-XA-DS	No	ZAOT	A	Double-Sided
5	noDF-XA_24mg	No	P.E.	В	Single-Sided

Table 4 Tested XA configurations at CIEMAT site.

3 Simulation Method

The XA PDE was measured at the Physics Department of the University of Naples Federico II and INFN. The photodetector module was placed horizontally inside a cryostat capable of holding up to 1 t of LAr. Figure 14 shows a layout of the setup. The XA photodetector module is placed horizontally on top of a metal frame held by four stainless steel rods fixed to the dome of the cryostat. Thermal insulating spacers connected the cryostat dome to the metal bars, preventing thermal conduction between the metal plate and the cryostat. A thermal stainless steel shield was placed a few centimetres away from the dome flange to reduce the thermal exchange due to the cold gaseous argon evaporating from the bulk of the liquid.

The inner walls of the cryostat were lined with black Delrin material and hung to a stainless steel thermal shield improving optical insulation and avoiding the reflection of photons from the stainless steel wall of the cryostat. With the same purpose, a Delrin disk was placed at the bottom side of the shield. The cryostat was filled with LAr with a level of contamination of the order of ~ 5 ppm (< 1.5 ppm N_2 , < 1 ppm H_2O , < 1 ppm O_2 and others). The LAr was filtered using an in-line Trigon (Engelhard Q5-Cu0226) purifier, reducing the amount of oxygen diluted in the LAr at the level of tenths of ppb or less. Before filling, the cryostat was pumped to make a vacuum of ${\sim}1\times10^{-3}\,\mathrm{mbar}$ after some cycles of pumping and purging with gaseous argon to reduce the contribution of outgassing. The cryostat was filled up to a height of 20 cm above the XA.

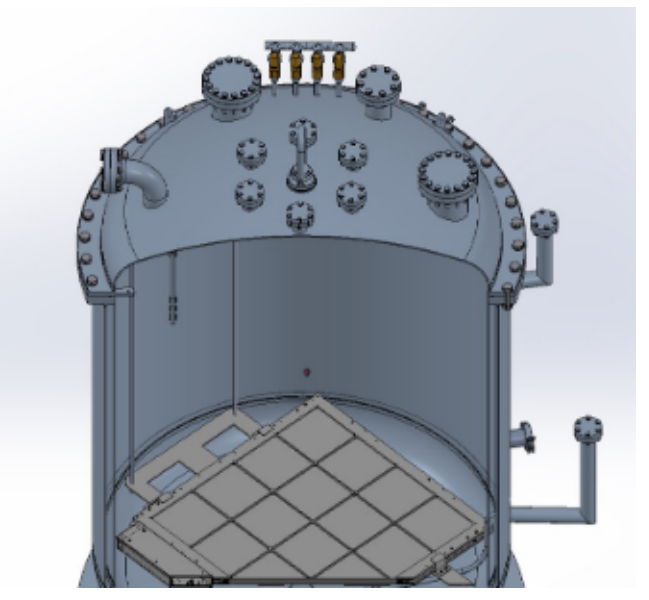
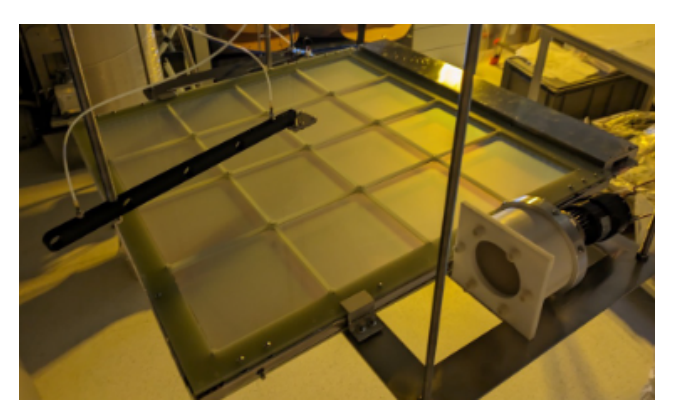


Fig. 14 Cryostat for XA PDE measurement at Naples' setup.



 ${f Fig.~15}$ View of the XA, PMT, and source holder from Naples' setup.

To monitor the liquid argon purity, a TPB-coated photomultiplier tube (Hamamatsu R11065 [18]) was used to measure the slow component of the liquid argon scintillation time profile. An optical fiber was used to drive pulsed laser flashes inside the cryostat to perform the calibration of the XA module. A 250 Bq activity ²⁴¹Am source was placed above the XA in an arm connected to a motion feedthrough, allowing the source to be changed in position with respect to the XA. The motion system was able to vary linearly the distance from the XA and rotate the arm where the source was placed, providing to radiate a large portion of the photosensor (see Table 5). Alpha particles decaying from the ²⁴¹Am produced enough amount of scintillation light for the final evaluation of the PDE. A detailed view of the setup is presented in Figure 15.

The data was digitised using a CAEN V1725, with 14-bit ADC and a sampling frequency of 250 MHz.

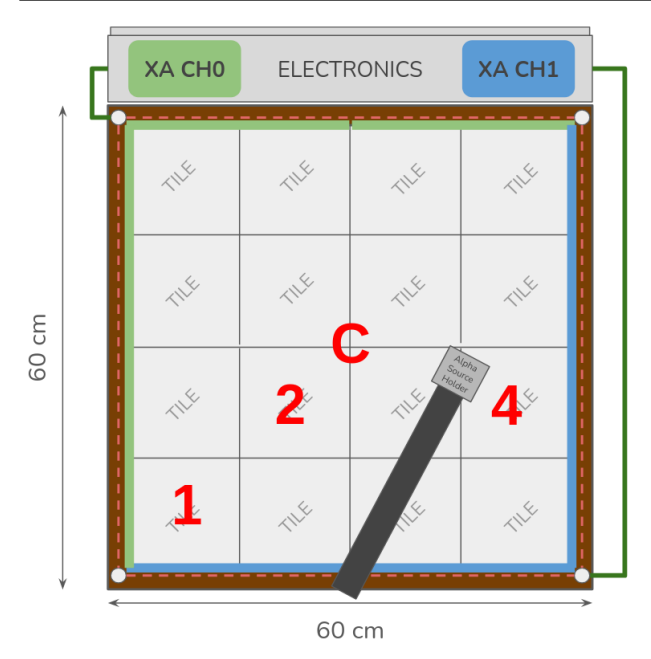


Fig. 16 XA channel arrangement in relation to the four reference positions of the alpha source.

Measurement Source Positions				
Position	Position x (cm)			
1	22	21		
2	10.5	5		
$^{\mathrm{C}}$	0	0		
4	-22.5	3		

Table 5 Spatial coordinates of each Americium source position in relation to the centre as implemented for the simulation method in Naples' setup.

Each channel reads two sides of the XA and a schematic can be seen in Figure 16.

3.1 Setup Simulation

In order to estimate the PDE of the XA, it is necessary to compare the number of detected PEs with the number of photons produced by scintillation reaching the sensor's optical window. The key difference between this method and the previously presented reference method is that this simulation is required to provide the absolute number of true photons, instead of the relative value. This method may be more challenging due to the uncertainties in the optical properties of the components at CT and their implementation in a MC simulation. The estimation of the number of photons was performed using a Geant4 simulation. The different position configurations of the alpha source used during the measurement (four positions in the plane and three different heights) were simulated. To estimate the error,

the source position was varied by 0.5 cm in x, y and z directions. Figure 17 shows the simulated setup. From the simulation, one can extract the expected response of the XA in terms of photon–collection. Figure 18 shows the mapping of the photons arriving at the XA optical window, where the red squares are the optical window. The simulation was performed using a MC approach, where the photons were generated isotropically from the source and propagated through the LAr medium until they reached the XA. The simulation is shown in Figure 19.

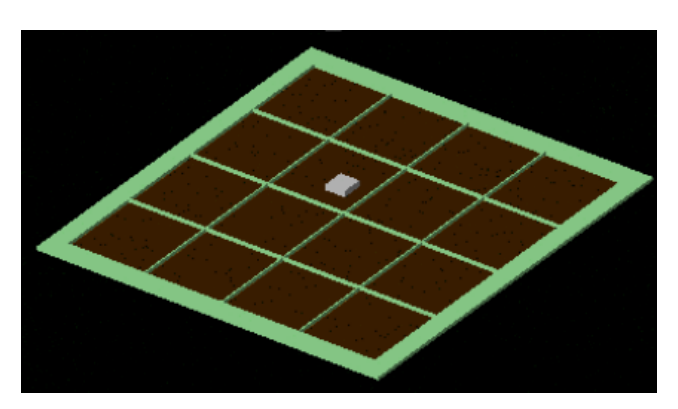


Fig. 17 Layout of the Geant4 simulation.

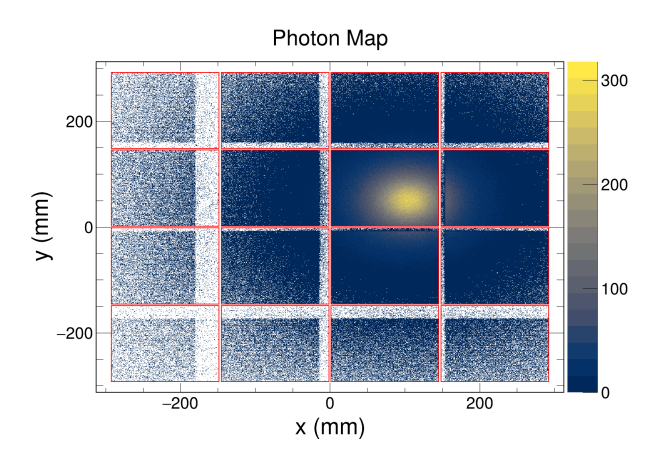


Fig. 18 Mapping of the photons arriving at the XA, where the red squares are the optical window. The source is located at position 2 and height of 5 cm. The presence of the shadow region is due to the photons coming from the source hitting the grids of the device For the source placed 5 cm away, the ratio between photons hitting the grid and photons reaching the optical window is approximately 15%.

The Equation 4 is used to fit the charge spectrum [25], which is the sum of two exponential functions multiplied by a complementary error function.

$$y[q] = \sum_{i=1}^{2} A_{i} \cdot \exp\left(\frac{q - u}{\tau_{i}} + \frac{\sigma_{i}^{2}}{2\tau_{i}^{2}}\right)$$
$$\cdot \operatorname{erfc}\left(\frac{1}{\sqrt{2}} \left(\frac{q - u}{\sigma_{i}} + \frac{\sigma_{i}}{\tau_{i}}\right)\right) \tag{4}$$

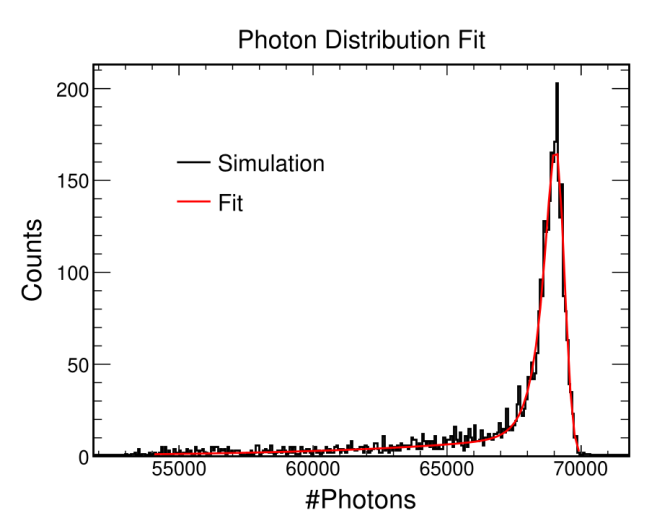


Fig. 19 Example of the number of photons reaching the optical window.

The A_1 and A_2 values are the renormalisation factors of both peaks, the u is the central position of the peak, σ_1 and σ_2 are the apertures of both peaks, and τ_1 and τ_2 are the values responsible for the long tail.

3.2 Computation Strategy

In the case of the simulation method, to evaluate the PDE, the following calculation is performed:

$$PDE_{XA}^{\text{simulation}} = \frac{PE_{XA}' \cdot f_{XA}^{\text{XT}}}{MC^{\text{photons}}} \cdot \frac{1}{f^{\text{bending}}} \cdot \frac{1}{f^{\text{purity}}}, \quad (5)$$

where $f^{\rm purity}$ is the purity correction of the liquid argon and $f^{\rm bending}$ is an additional correction required to compensate for the bending of the XA light guide.

The LAr purity is a critical parameter to evaluate for the simulation method due to the presence of contaminating impurities that affect the absolute light propagation. Specifically, nitrogen and oxygen concentrations as low as a few parts per million (ppm) significantly reduce the total scintillation light reaching the XA detector [26]. This effect can be quantified by analysing the slow scintillation component of liquid argon (τ_{slow}), as nitrogen and oxygen quench its intrinsic decay time of (1660 ± 100) ns [27]. In Naples' setup, the amount of O_2 is strongly reduced by the use of the argon filter, while the N_2 impurities can still affect the

liquid argon scintillation light. To determine the slow component, the average waveform was calculated using signals from a Hamamatsu PMT R11065, operated at $1500\,\mathrm{V}$ and triggered by cosmic muon interactions in LAr.

The muons were selected based on the region with a prompt light ratio close to 0.4. By calculating the prompt ratio, defined as the ratio of the fast integral over the total integral, it is possible to select a region where argon nuclear recoils occur more frequently than electron recoils, allowing for the separation of alpha particles from cosmic muons. This is because alpha particles are expected to interact more via nuclear recoil than muons. The prompt ratio is calculated according to Equation 6:

$$Prompt = \frac{\int_{t_0}^{t'} v(t)dt}{\int_{t_0}^{T} v(t)dt}$$
 (6)

where v(t) is the measured signal, t_0 is the start time of the waveform, and T is the waveform end time. The parameter t' represents the upper limit for the fast integral, which for the PMT signal was chosen to be on the order of $0.5 \,\mu s$.

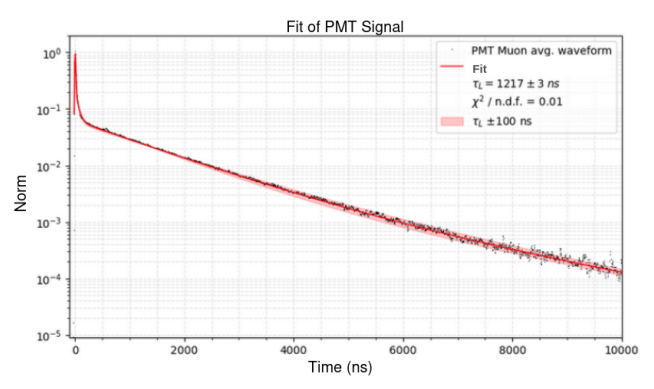


Fig. 20 Fitted LAr slow component of the scintillation light captured by the PMT.

The value of the slow component (τ'_{slow}) was obtained by fitting the tail of the result of the convolution of the slow component with a Gaussian filter (simulating the electronics response) and with the TPB response [28]. The fitted average waveform is shown in Figure 20 and the value obtained is (1217 ± 50) ns. The liquid argon purity correction factor is therefore estimated with the equation:

$$f^{\text{purity}} = A_{\text{fast}} + A_{\text{slow}} \cdot \frac{\tau'_{slow}}{\tau_{slow}} = 0.94 \pm 0.06$$
 (7)

where the proportion between fast and slow components was calculated using the mean values obtained at [29,30,31].



Fig. 21 Bending of the XA WLS–LG after data–taking campaign

Apart from the purity correction, an unexpected additional correction factor was found to be needed to account for the bending of the light guide found after the measurements. During the inspection phase, it was discovered that the light guide had bent and there was a significant misalignment between the light guide plane and the SiPM flex boards (see Figure 21). This issue can be attributed to the fact that during the measurement phase, the XA was positioned horizontally, with the light guide supported on only two sides rather than all four. As this was one of the first XA prototypes, the problem observed in this test led to the inclusion of additional support points for the light guide in the design, which were improved in subsequent devices. This issue was not observed in CIEMAT's setup due to the vertical orientation of the measurement, which prevented this bending from affecting the data.

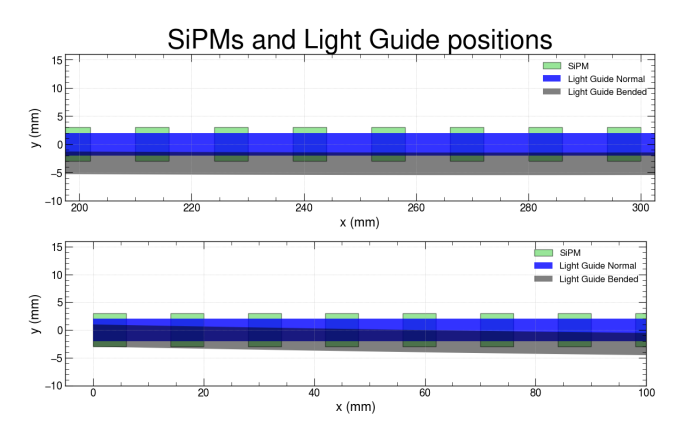


Fig. 22 Schematic of the bending of the light guide XA. The green squares represent the internal SiPMs, each with a side length of 6 mm and centre—to—centre spacing of 14 mm. The blue part represents the unbent light guide configuration, while the black region represents the bent light guide.

To account for this issue, the misalignment shifts of the SiPMs relative to the centre of the light guide along each side were carefully measured. A representation of the misalignment is shown in Figure 22, where the central and the edge part (top and bottom) of the XA components are schematized. A vertical shift of approximately 5 mm was observed at the midpoint, and a vertical offset of about 2 mm was noted at the edges.

Due to the close placement of the SiPM surfaces relative to the edges of the light guide, a correction factor was implemented to compensate for bending effects and adjust the photon collection efficiency. The bending was modelled using the catenary equation, which is a hyperbolic cosine function:

$$y = a \cdot \cosh(x/b) + c. \tag{8}$$

The ratio of the areas aligned with the SiPMs in the bent versus unbent light guide configurations was calculated to be $f^{\rm bending} = 0.58 \pm 0.08$. It is important to note that this bending correction was characterised after the measurements, and might have been more dramatic during the data taking. Nevertheless, we provide an absolute PDE value based on the assumption that this correction holds.

4 Data Analysis & XA Characterization

In the following, we present the common analysis steps of the data acquired at both CIEMAT and INFN setups. The XA has been operated with voltage values of $30.5\,\mathrm{V},\,31.5\,\mathrm{V},\,33\,\mathrm{V}$ and $34\,\mathrm{V},$ corresponding to $3.5\,\mathrm{V},\,4.5\,\mathrm{V},\,6\,\mathrm{V}$ and $7\,\mathrm{V}$ overvoltage, respectively².

4.1 XA Calibration

A standard set of data runs has been obtained and analysed (see Table 6). The calibration and α –source runs are used in the PDE computation, and the muon and noise runs monitor the purity and stability of the setup. The triggering scheme is provided by a pulsed generator that simultaneously feeds the laser and the DAQ. The result is a set of aligned waveforms with a defined time correlation.

Run Type Summary

Type	Source	Trigger	Signal
Calibration	Laser	External	Pulsed
$lpha ext{-source}$	$^{241}\mathrm{Am}$	DAQ	Scintillation
Muons	Cosmic	DAQ	Scintillation
Noise	None	Random	None

Table 6 Main run types and their characteristics.

Figure 23 shows an example waveform for a calibration run of the XA. Three distinct pulse regions can be recognised.

Determining the SPE charge is a necessary first step in calculating the absolute gain of a photosensitive

 $^{^2}For$ reference, $3.5\,V,\,4.5\,V$ and $7\,V$ overvoltage correspond to $40\%,\,45\%$ and 50% efficiency of the mounted SiPMs at room temperature.

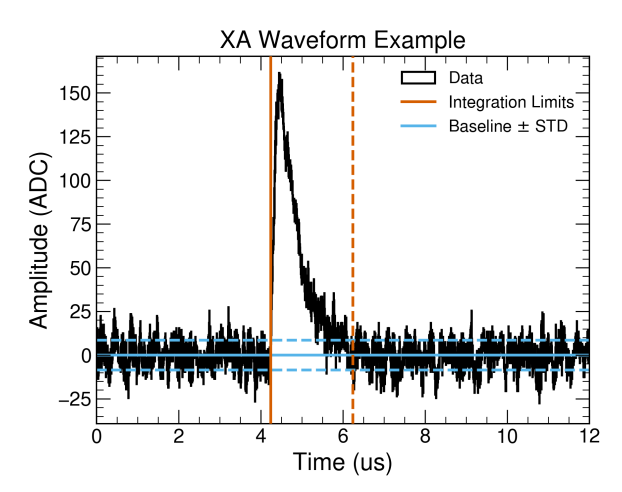


Fig. 23 $\,$ XA signal example from a calibration run with 4.5 V overvoltage.

setup. This variable goes directly into the gain computation. It is obtained from a charge histogram of a calibration run, where the external light source is set to deliver low–intensity pulses of light. This results in waveforms containing only a few PEs (see Figure 24).

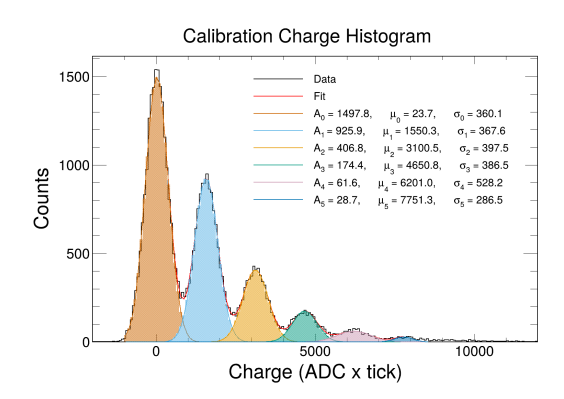


Fig. 24 Charge histogram for channel 1 with an overvoltage of $4.5\mathrm{V}$

The waveforms are normalized by integrating the pretrigger region to determine a baseline value that is subtracted from the full array. Then, the charge integral is calculated on a fixed time window after the signal's rise—time (see Figure 23). Finally, to determine the SPE gain, one computes the charge difference between two consecutive SPE peaks on the charge histogram. The charge histograms are computed and fitted individually with Gaussian curves for each XA readout channel. The evaluated gain of the XA as a function of the overvoltage is shown in Figure 25.

The signal-to-noise ratio is determined as shown in the equation 9:

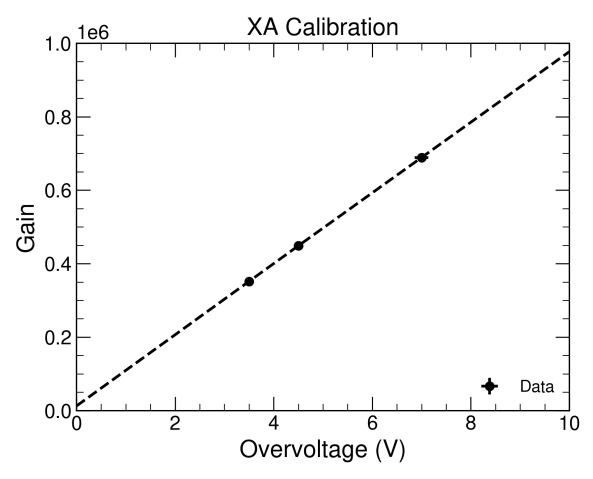


Fig. 25 Gain versus bias voltage, as tested by CIEMAT, for the baseline XA configuration. The dashed line shows the function computed for the best–fit parameters.

$$SNR = \frac{\mu_1}{\sqrt{\sigma_0^2 + \sigma_1^2}}. (9)$$

where μ_1 is the mean of the first SPE_{charge} distribution and σ_i are the corresponding Gaussian sigmas for the pedestals and first SPE peak.

From the same charge histogram, a cross-talk result can be obtained by plotting the signal density (normalised charge of the Gaussian fits) over the number of PEs. If no additional pulse happened, the distribution of the number of single photon electrons per event would follow a normal Poisson distribution with mean λ . Due to the existence of the cross-talk, the distribution follows a generalised Poisson distribution with mean λ and a crosstalk probability $P^{\rm XT}$ [32]. To generate the distribution of events with a given number of PEs, the number of events corresponding to each Gaussian in the single PE charge histogram is first obtained. The spectrum is then fitted using the distribution described in Equation 10.

$$f(n, \lambda, P^{XT}) = \frac{e^{-\lambda}}{n!} \sum_{i=0}^{n} B_{i,n} \left[\lambda \cdot (1 - P^{XT}) \right]^{i} \cdot (P^{XT})^{n-i}$$

$$B_{i,n} = \begin{cases} 1 & \text{when } i = 0 \text{ and } n = 0 \\ 0 & \text{when } i = 0 \text{ and } n > 0 \\ \frac{n!(n-1)!}{i!(i-1)!(n-i)!} & \text{otherwise} \end{cases}$$
(10)

The average of the distribution is determined by $\lambda \cdot \left(1 + \frac{P^{\text{XT}}}{1 - P^{\text{XT}}}\right)$. Therefore, to obtain the real distribution of PEs (without XT effects) is necessary to multiply the average by the factor f^{XT} in Equation 11.

$$f^{\rm XT} = \frac{1}{1 + K_{\rm dup}}$$
 with $K_{\rm dup} = \frac{P^{\rm XT}}{1 - P^{\rm XT}}$. (11)

This procedure is the so-called Vinogradov method, and a specific implementation of a fit to extract the XT probability value can be seen in Figure 26.

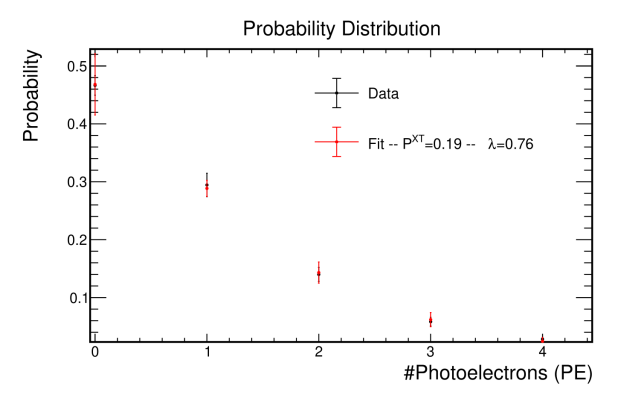


Fig. 26 Example Crosstalk evaluation (4.5 V OV)

The final set of characterisation data extracted from the calibration runs is summarised in Table 7.

Gain $(\cdot 10^5)$ S/N P ₂	XA Calibration	(DF–XA)	
	Gain $(\cdot 10^5)$	S/N	Ру

OV (V)	Gain $(\cdot 10^5)$	S/N	P_{XT} (%)
3.5	3.52 ± 0.03	3.1 ± 0.8	12.8 ± 0.3
4.5	4.48 ± 0.04	3.7 ± 0.9	18.4 ± 0.4
6.0	5.75 ± 0.04	4.1 ± 0.2	29.0 ± 0.2
7.0	6.89 ± 0.06	5.4 ± 1.3	32.6 ± 0.7

Table 7 Weighted average XA calibration results from combined analysis of both XA channels.

4.2 Scintillation Charge Analysis

The alpha particle scintillation spectrum has been measured with the XA to estimate the device's PDE. For this measurement, the light of the americium source needs to be triggered and evaluated. In the case of the reference method, the characterisation box ensures the fixed position of the americium source with respect to the photosensitive areas of the XA and the reference sensors. Additionally, the reference SiPMs provide a coincidence trigger that excludes all noise from the analysis sample. Due to the reduced size of the box, any cosmic interaction is also quite constrained and, if present, easily removable with an amplitude cut.

For the simulation method, the position of the americium source holder needs to be calibrated. To ensure its stability, the source height has been adjusted to different values above the XA (5 cm,

10 cm and 15 cm). At each height, measurements were taken at four different positions, as shown in Figure 16. The alpha signal is obtained by triggering on one channel, and the charge is reconstructed by independently integrating both waveforms over a 6.6 µs window. Additionally, the fast integral is calculated by integrating over a $0.92 \, \mu s$ region (t'), for determining the prompt light ratio. An example of the excellent alpha/muon separation that this method provides is shown in Figure 27.

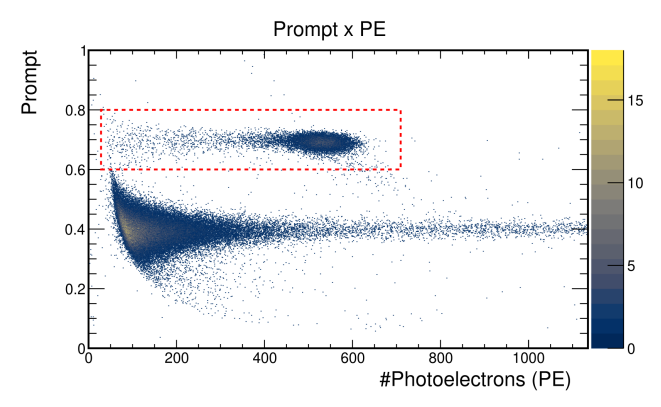


Fig. 27 Prompt distribution as a function of the total charge. In red is the selected region due to the scintillation of alpha particles.

The signal induced by alpha particles was selected with a cut on events with Prompt > 0.6. After the selection, the charge spectrum results in a Gaussian with a long tail extending toward lower energies due to edge effects of the source holder, as shown in Figure 28. In order to obtain the peak's central value, the distribution of the number of photons obtained with the simulation was fitted with the same equation 4 used for the MC simulation.

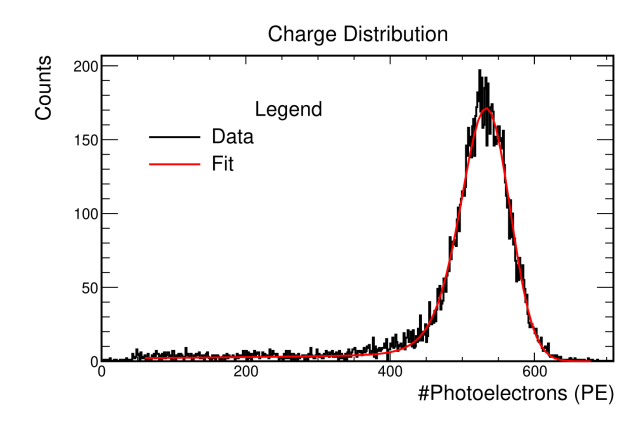


Fig. 28 Alpha's charge spectrum (SiPM overvoltage 7V and alpha source at position 2 and 15 cm above the XA), from channel 0.

In the case of the reference method, the charge spectrum is obtained by integrating the waveforms of the reference XA channels individually. Due to the required triggering of both reference SiPMs and the symmetric position of the alpha source with respect to the characterisation box, the charge spectrum has been simply fitted to a Gaussian.

5 Results

As already described, there are three main XA design choices that have been evaluated in this work: SS vs. DS performance, DF effect on the PDE and WLS–LG improvements. In the following, we discuss the repeated measurement of the baseline XA configuration with both methods, the stability of the setups by evaluating the repetitiveness of the measurements, and we give a detailed description of the uncertainty treatment.

5.1 Baseline PDE XA Results

The PDE values for the baseline SS XA model are shown in Table 8. These values are computed as the weighted mean from the results of the characterisation boxes and the source heights and analysis positions for the reference and simulation methods, respectively. The individual results are shown in Figure 29 and Figure 30. As can be seen, these results show a minor but consistent divergence between the two methods, which is expected due to the already mentioned limitations of the bending correction for the simulation method. This correction was not required for CIEMAT's measurements thanks to the optimised XA mechanical frame, which ensured the alignment between the WLS-LG and the SiPMs in all positions.

Photon Detection Efficiency

OV (V)	CIEMAT	INFN Naples
3.5	$3.2 \pm 0.2 \%$	
4.5	$3.7 \pm 0.3 \%$	$3.1 \pm 0.5 \%$
6.0		$3.6 \pm 0.5 \%$
7.0	$4.7\pm0.3~\%$	$4.0\pm0.6~\%$

Table 8 PDE as a function of OV for the baseline SS XA compared between the two sites.

Both for the reference and simulation methods (see Figures 29 and 30), one can observe the expected increase in PDE for source positions that are closer to the device's edges. By analysing both the PDE dependence on source height and position with respect to the XA's geometrical centre, one can evaluate the variance associated with this measurement from which a central value is extracted, and the uncertainty is computed.

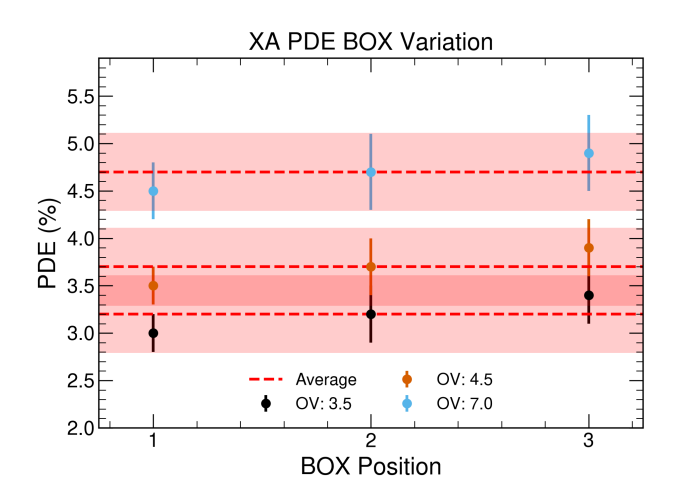


Fig. 29 Baseline XA PDE from the reference method. Showing the PDE as a function of characterisation box position. The dashed line represents the average position—weighted value of the PDE.

In the following, we list the evaluated parameters that have been considered in the error propagation formula of the reference method with their relative error values. The final uncertainty is computed as the square root of the squared sums of the individual contributions:

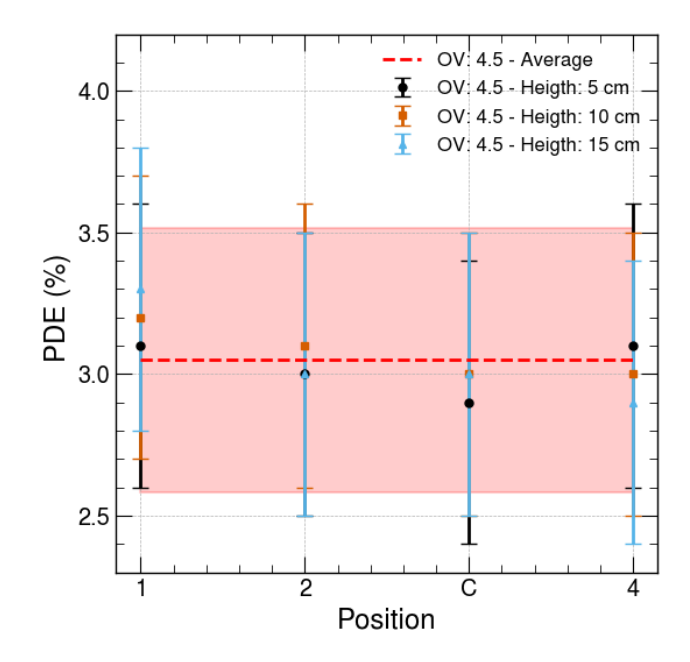


Fig. 30 Baseline XA PDE from the simulation method. Showing example source height scan for $4.5\,\mathrm{V}$ overvoltage.

- Reference SiPM PDE (8.7%). Obtained from publication [20].
- Reference SiPM PE count (~ 2%). Computed from the common error propagation of the gain factor (linear fit) and the combined PE count distribution of the pair of sensors in each characterisation box (Gaussian fit).
- Reference SiPM XT Factor ($\sim 2\%$). Statistically evaluated from the spread in calibration data.
- Geometric Factor (1.5%). Obtained from simulation by evaluating the impact of mechanical distortions in the characterisation boxes, which have been measured after each data—taking campaign.
- XA XT Factor ($\sim 1\%$). Obtained from calibration data.
- XA PE count ($\sim 1\%$). Computed from the common error propagation of the gain factor (linear fit) and the average charge count (Gaussian fit).

In the values presented for the simulation method, the error propagation has followed a similar strategy with the corresponding factors presented in previous sections and summarized in the following list:

- XA Gain ($\sim 1\%$). From data analysis, including error propagation across multiple runs.
- XA XT Factor ($\sim 10\%$). From data analysis, error propagation, and cross-checks between independent runs.
- LAr Purity: $f^{\rm purity}$ ($\sim 6\%$). From data analysis and results reported in the literature.
- Bending Factor: $f^{\rm bending}$ ($\sim 14\%$). From direct measurement uncertainties on the bar geometry.
- Number of Photons (simulation) ($\sim 4\%$). From variations in source position, light yield, and analysis of simulated data.

We conclude that the final uncertainty of the reference PDE values is dominated by the uncertainty in the PDE of the reference SiPMs. In the case of the simulation method, the large uncertainty attributed to the bending correction of the INFN setup has lead to a larger uncertainty in the final PDE value. The final uncertainty for the reference method is $\sim 9\%$ and for the simulation method, $\sim 15\%$.

5.2 Stability & Repetitivity

Having validated the XA design and the measurement methods, the next step is to evaluate the stability and reproducibility of the measurements. This is crucial for ensuring that the PDE results are consistent over time and across different experimental setups. The gain monitoring of the sensors, as well as a stable and consistent PDE evaluation during all data runs, has been deemed necessary to consider a campaign successful.

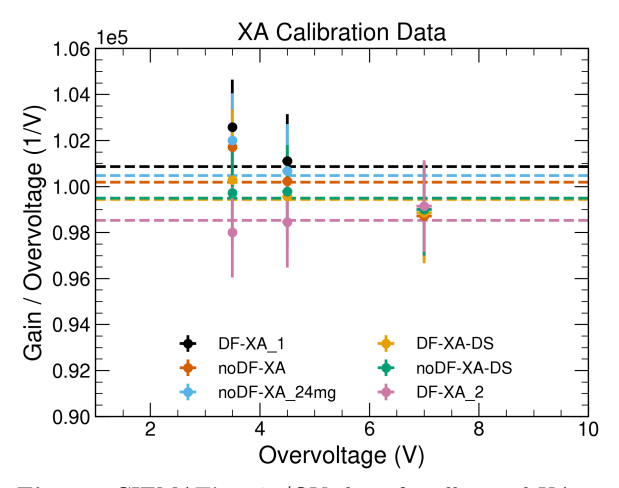


Fig. 31 CIEMAT's gain/OV slope for all tested XA configurations. Dashed lines represent the weighted average.

In the case of CIEMAT's results, these have been computed for up to three individual sets of runs for each XA configuration. These sets of repeated data have been acquired to guarantee the reliability of the results presented in this work. The results for the gain/OV slope of the XA measurements are shown in Figure 31. The results show a consistent gain/OV slope across all configurations, indicating that the experimental setup is operated at stable conditions and that the electronics of the XA are not drifting over the ~1 year period of data taking.

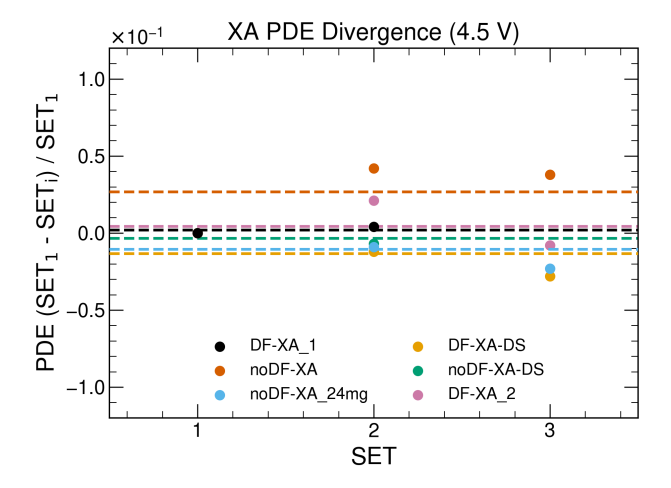


Fig. 32 Relative PDE deviation with respect to the first evaluated value for all XA configurations at $4.5\,\mathrm{V}$ overvoltage. The dashed lines represent the mean of the deviations.

Regarding the repeated PDE computation, Figure 32 presents a set of results (for $4.5\,\mathrm{V}$ OV) that show the relative divergence of the PDE values for the second and third sets for all XA configurations with respect to the first computed value. The relative deviations are computed as $(\mathrm{PDE}_{\mathrm{XA}}^{i} - \mathrm{PDE}_{\mathrm{XA}}^{1})/\mathrm{PDE}_{\mathrm{XA}}^{1}$, where $\mathrm{PDE}_{\mathrm{XA}}^{i}$ is the PDE value for the *i*-th set and $\mathrm{PDE}_{\mathrm{XA}}^{1}$ is the first evaluated value of the PDE. As can be observed, the relative PDE variations fall within a 3% mean range that lies reasonably below the computed uncertainty of the XA PDE measurement (\sim 9%).

5.3 XA Configuration Comparison

Finally, we evaluate the impact of the measured PDE values on the XA design choices and optimisations. Table 9 shows the values for the tested XA configurations. Notice that the first configuration (also evaluated with the simulation method) has the lowest uncertainty thanks to the repeated measurement.

VD-XA PDE Results (%)

	Config	OV 3.5 V	OV 4.5 V	OV 7 V
	DEWA	22102	0 7 1 0 0	4 7 1 0 0
_	DF-XA	3.2 ± 0.2	3.7 ± 0.3	4.7 ± 0.3
2	DF-XA-DS	3.5 ± 0.3	4.0 ± 0.4	5.0 ± 0.5
3	noDF-XA	3.9 ± 0.4	4.5 ± 0.4	5.8 ± 0.6
4	noDF-XA-DS	3.8 ± 0.4	4.5 ± 0.4	5.6 ± 0.6
5	$noDF-XA_24mg$	3.6 ± 0.4	4.3 ± 0.4	5.5 ± 0.6

Table 9 Results for the XA absolute PDE for all tested configurations and OV values.

To better represent the differences between the design changes among the configurations, Table 10 shows the relative PDE values computed as $(PDE_{XA}^{i} - PDE_{XA}^{j})/PDE_{XA}^{j}$. The data for the three distinct overvoltage measurements are shown in Table 10, and the average is taken to increase the statistical significance. Notice that this can be safely performed because the overvoltage choice should have no impact on the relative PDE at the evaluation.

Regarding the comparison between noDF and DF devices (columns two and three in Table 10), one concludes that the XAs without DF coating present a noticeable increase in PDE (18% & 11%) to their SS and DS baseline counterparts. As anticipated in Section 1, these results were expected and have hereby been confirmed and characterised, strengthening the methodology and analytic tools developed for the optimisation and development procedures.

Additionally, we observe slight differences that fall close to the measurement uncertainty and express

XA PDE Comparison							
	noDF vs. DF		DS vs. SS				
OV(V)	SS	DS	DF	noDF			
2.5	10 907	0 1 207	7 207	0 1 207			
3.5	$18 \pm 3\%$	$8 \pm 3\%$	$7 \pm 3\%$	$-2 \pm 3\%$			
4.5	$17 \pm 3\%$	$12 \pm 3\%$	$3 \pm 3\%$	$-2 \pm 3\%$			
7.0	$20 \pm 3\%$	$12 \pm 3\%$	$3\pm3\%$	$-4 \pm 3\%$			
Mean	18.4%	10.6%	4.2%	-2.6%			

Table 10 Relative improvements for the XA's absolute efficiency for different configurations and OV values.

different tendencies between configurations with and without a dichroic filter for the Single- and Double-Sided comparison (columns four and five in Table 10). The performance of both configurations seems compatible, and we conclude that the VIKIUTI present in the Single–Sided configuration to substitute the substrates is providing a low recollection performance. The fact that both configurations present similar results points to the overwhelming capture preference of photons trapped through internal reflection in the WLS-LG. In other words, efforts to collect photons that have escaped the WLS-LG due to the isotropic emission that can exceed the medium's critical angle do not seem to operate with high enough efficiency to result in measurable improvements. Beyond the compatibility conclusion, it is out of the scope of this publication to determine if the slight divergence observed is caused by manufacturing changes or an underlying difference in the configurations.

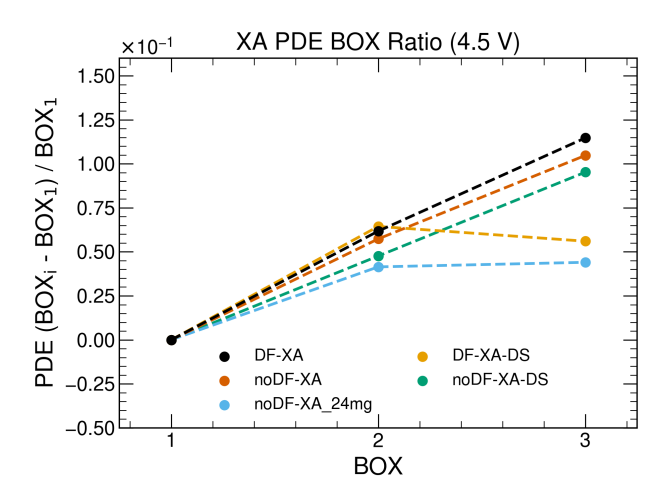


Fig. 33 CIEMAT's PDE measurements as a function of characterisation box position for the reference OV value of $4.5\,\mathrm{V}.$

Lastly, the PDE results for the $24 \,\mathrm{mg \, kg^{-1}}$ chromophore concentration and $5.5 \,\mathrm{mm}$ width WLS–LG configuration show no improvement in the absolute

PDE with respect to the equivalent configuration without DFs. The difference is not statistically significant and does not warrant further investigation at this time. Nevertheless, one can observe a different behaviour by plotting the position–dependent relative PDE for the different configurations (see Figure 33). The use of the alternative WLS–LG does seem to provide a flatter response across the different box positions. This is a desirable feature for the DUNE PDS, as it allows for a more uniform light collection efficiency across the detector's volume, which is crucial for an accurate event reconstruction. Further simulation and optimisation of the XA design may be required to fully understand the potential benefits of different WLS–LG configurations.

6 Conclusions

The work presented in this publication provides a comprehensive analysis of the PDE performance for the XA configuration proposed for the DUNE FD VD PDS. It highlights the successful implementation of two distinct evaluation methods, named reference and simulation, to measure the absolute PDE of the baseline configuration described in Section 1.

First, we have proven the compatibility between the measurements of the baseline XA configuration. The reference method has provided an absolute PDE of $3.7\pm0.3\%$ and the simulation method a value of $3.1\pm0.5\%$ at OV 4.5 V. These results confirm the meeting requirements of the device for DUNE's physics scope and prove the effectiveness of the design and optimisation strategies employed in the XA development by demonstrating a significant improvement in PDE compared to the previously implemented FD Horizontal Drift (HD) XA [33]. As a benchmark, the HD results have a PDE times Surface over #SiPM of 26 while the here presented PDE yields a value of 83, which is a factor of 3.2 higher for this figure of merit.

Second, having validated the results of the reference method, we present additional measurements carried out at CIEMAT. These have been presented in Table 9 and reveal the compatibility of results between SS and DS measurements. Additionally, we confirm the improvement in PDE predicted for configurations without DF and find the improvement to be 18% & 11% for SS and DS configurations, respectively. The highest measured PDE value has been $4.5\pm0.4\%$ OV at $4.5\,\mathrm{V}$ corresponding to the SS configuration without DF. Therefore, we recommend to remove the DF coating from the baseline XA in DUNE FD VD design.

Finally, we did not observe the predicted effects in PDE for the WLS-LG of $24 \,\mathrm{mg\,kg}^{-1}$ chromophore

concentration & 5.5 mm width. This configuration does have a flatter PDE curve (with a Standard Deviation (STD) of 2%) across the measured characterisation box positions (described in Section 2), but the absolute PDE is not improved. This suggests that further optimisation of the XA simulation may be required to fully understand the potential benefits of different WLS–LG configurations.

The absolute PDE of the XA is a crucial parameter for the DUNE PDS, as it directly influences the detector's sensitivity to VUV light and, consequently, its ability to accurately reconstruct neutrino interactions. The results presented in this publication confirm some expected improvements in PDE resulting from simulation studies and set a solid foundation for future DUNE PDS developments.

References

- DUNE Collaboration, "Deep Underground Neutrino Experiment (DUNE), Far Detector Technical Design Report, Volume I Introduction to DUNE," JINST, vol. 15, no. 08, p. T08008, 2020.
- DUNE Collaboration, "Deep underground neutrino experiment (dune), far detector technical design report, volume ii: Dune physics," TBD, 02 2020.
- DUNE Collaboration, "Supernova neutrino burst detection with the Deep Underground Neutrino Experiment," 2021.
- A. Machado, E. Segreto, D. Warner, A. Fauth, B. Gelli, R. Máximo, A. Pissolatti, L. Paulucci, and F. Marinho, "The x-arapuca: an improvement of the arapuca device," *Journal of instrumentation*, vol. 13, no. 04, p. C04026, 2018.
- 5. M. A. Arroyave, B. Behera, F. Cavanna, A. Feld, F. Guo, A. Heindel, C. K. Jung, K. Koch, D. L. Silverio, D. A. M. Caicedo, C. McGrew, A. Paudel, W. Pellico, R. Rivera, J. R. Rondon, S. Sacerdoti, P. Shanahan, W. Shi, D. T. Muñoz, D. Totani, C. Uy, C. Vermeulen, and H. V. de Souza, "Characterization and novel application of power over fiber for electronics in a harsh environment," 2024.
- T. Doke, A. Hitachi, J. Kikuchi, K. Masuda, H. Okada and E. Shibamura, "Absolute Scintillation Yields in Liquid Argon and Xenon for Various Particles," mar 2002.
- T. Heindl, T. Dandl, M. Hofmann, R. Krücken, L. Oberauer, W. Potzel, J. Wieser and A. Ulrich, "The scintillation of liquid argon," oct 2010.
- A. Hitachi, T. Takahashi, N. Funayama, K. Masuda, J. Kikuchi, and T. Doke, "Effect of ionization density on the time dependence of luminescence from liquid argon and xenon," *Phys. Rev. B*, vol. 27, pp. 5279–5285, May 1983.
- DUNE Collaboration, "The DUNE Far Detector Vertical Drift Technology. Technical Design Report," Journal of Instrumentation, vol. 19, p. T08004, aug 2024.
- DUNE Collaboration, "Deep Underground Neutrino Experiment (DUNE), Far Detector Technical Design Report, Volume IV: Far Detector Single-phase Technology," 2020
- N. Nijegorodov, W. Downey, and M. Danailov, "Systematic investigation of absorption, fluorescence and laser properties of some p-and m-oligophenylenes," Spectrochimica Acta Part A: Molecular and Biomolecular Spectroscopy, vol. 56, no. 4, pp. 783–795, 2000.
- Vikuiti™. Enhanced Specular Reflector (ESR).
- 13. B. Abi *et al.*, "First results on ProtoDUNÉ-SP liquid argon time projection chamber performance from a beam test at the CERN Neutrino Platform," *JINST*, vol. 15, no. 12, p. P12004, 2020.
- 14. Glass to power. (G2P) Wavelength Shifter bar.
- 15. Fondazione Bruno Kessler. (FBK) SiPM technology.
- N. Gallice, A. Zani, P. Sala, M. Lazzaroni, M. Citterio, and A. Andreani, "Development of a design for sipms readout in cryogenic environment for large area photon detectors," in 2021 IEEE International Instrumentation and Measurement Technology Conference (I2MTC), pp. 1–6, IEEE, 2021.
- 17. DUNE Collaboration, "Fd-vd photon collectors: Design, optimization and characterization." Manuscript in preparation, 2025.
- Hamamatsu Photonics K.K. (HPK). Multi-Pixel Photon Counters (MPPCs/SiPMs) Photomultiplier Tube (R11065-20A).

- T. Pershing, J. Xu, E. Bernard, J. Kingston, E. Mizrachi, J. Brodsky, A. Razeto, P. Kachru, A. Bernstein, E. Pantic, et al., "Performance of hamamatsu vuv4 sipms for detecting liquid argon scintillation, 2022."
- L. Pérez-Molina, "Measurement of the photon detection efficiency of hamamatsu vuv4 sipms at cryogenic temperature," *Journal of Instrumentation*, vol. 19, no. 03, p. C03027, 2024.
- S. Vinogradov, T. Vinogradova, V. Shubin,
 D. Shushakov, and K. Sitarsky, "Probability distribution and noise factor of solid state photomultiplier signals with cross-talk and afterpulsing," in 2009 IEEE Nuclear Science Symposium Conference Record (NSS/MIC), pp. 1496–1500, IEEE, 2009.
- P. Nakarmi, I. Ostrovskiy, A. Soma, F. Retière,
 S. Al Kharusi, M. Alfaris, G. Anton, I. Arnquist,
 I. Badhrees, P. Barbeau, et al., "Reflectivity and pde of vuv4 hamamatsu sipms in liquid xenon," Journal of Instrumentation, vol. 15, no. 01, p. P01019, 2020.
- 23. E. C. Alamillo, M. C. Vázquez, P. R. Mendes, R. Á. Garrote, J. C. Anadón, C. Cuesta, A. De la Torre Rojo, I. Gil-Botella, I. M. Martín, M. M. Mendieta, et al., "Validation of electrodeposited 241am alpha-particle sources for use in liquified gas detectors at cryogenic temperatures," Applied Radiation and Isotopes, vol. 200, p. 110913, 2023.
- 24. CAEN. Tools for Discovery.
- S. Pommé and B. Caro Marroyo, "Improved peak shape fitting in alpha spectra," Applied Radiation and Isotopes, vol. 96, pp. 148–153, 2015.
- R. Acciarri et al., "Effects of nitrogen and oxygen contamination in liquid argon," Nuclear Physics B Proceedings Supplements, vol. 197, no. 1, pp. 70–73, 2009.
 11th Topical Seminar on Innovative Particle and Radiation Detectors (IPRD08).
- A. Hitachi, T. Takahashi, N. Funayama, K. Masuda, J. Kikuchi, and T. Doke, "Effect of ionization density on the time dependence of luminescence from liquid argon and xenon," *Phys. Rev. B*, vol. 27, pp. 5279–5285, May 1983.
- E. Segreto, "Evidence of delayed light emission of tetraphenyl-butadiene excited by liquid-argon scintillation light," *Physical Review C*, vol. 91, Mar. 2015.
- S. Kubota, M. Hishida, M. Suzuki, and J.-z. Ruan(Gen), "Dynamical behaviour of free electrons in the recombination process in liquid argon, krypton, and xenon," *Phys. Rev. B*, vol. 20, pp. 3486–3496, Oct 1979.
- M. Carvalho and G. Klein, "Luminescence decay in condensed argon under high energy excitation," *Journal of Luminescence*, vol. 18-19, pp. 487–490, 1979.
- 31. R. Acciarri et al., "Effects of nitrogen contamination in liquid argon," Journal of Instrumentation, vol. 5, p. P06003–P06003, June 2010.
- S. Vinogradov, T. Vinogradova, V. Shubin,
 D. Shushakov, and K. Sitarsky, "Probability distribution and noise factor of solid state photomultiplier signals with cross-talk and afterpulsing," in 2009 IEEE Nuclear Science Symposium Conference Record (NSS/MIC), pp. 1496–1500, 2009.
- 33. R. Álvarez-Garrote, C. Brizzolari, A. Canto, E. Calvo, C. Cattadori, C. Cuesta, A. de la Torre Rojo, I. Gil-Botella, C. Gotti, D. Guffanti, et al., "Measurement of the absolute efficiency of the x-arapuca photon detector for the dune far detector 1," The European Physical Journal C, vol. 84, no. 10, p. 1004, 2024.

Acknowledgements

The present research has been supported and partially funded by the Italian Ministero dell'Università e della Ricerca (PRIN 2017KC8WMB and PRIN 20208XN9TZ), by the European Union's Horizon 2020 Research and Innovation programme under Grant Agreement No 101004761 (AIDAinnova), by the European Union-Next Generation EU by MCIN/AEI/10.13039/501100011033 under Grants no. PID2019-104676GB-C31, No. PID2019-104676GB-C32 & CNS2023-144183 and PRE2020-094863 of Spain, and finally by the University of Ferrara (FIR2023), the BiCoQ Center of the University of Milano Bicocca and Leonardo Grant for Researchers in Physics 2023 BBVA Foundation, LEO23-1-9021.